ISIJ International, Vol. 64 (2024), No. 5, pp. 874–880
https://doi.org/10.2355/isijinternational.ISIJINT-2023-470

Multiscale Finite Element Analysis of Yield-point Phenomenon in Ferrite–Pearlite Duplex Steels

Shinnosuke YANAGAWA[1,2] and Ikumu WATANABE[1,2]*

1) Degree Programs in Pure and Applied Sciences, Graduate School of Science and Technology, University of Tsukuba, 1-1-1 Tennodai, Tsukuba, Ibaraki, 305-0006 Japan.
2) Center for Basic Research on Materials, National Institute for Materials Science, 1-2-1 Sengen, Tsukuba, Ibaraki, 305-0047 Japan.

(*Received December 12, 2023; Accepted January 14, 2024; Advance online published February 16, 2024; Published March 15, 2024; Originally published in Tetsu-to-Hagané, Vol. 110, 2024, No. 3, pp. 333–341*)

The yield-point phenomena in ferrite–pearlite duplex steels were investigated using multiscale computational simulations. In these multiscale simulations, the stress–strain relationship of the ferrite phase was characterized by an elastoplastic constitutive model considering the stress-drop behavior, and its material constants were determined by minimizing the residual error between a computational simulation and a tensile test experiment, where the yield-point phenomenon in a tensile test of ferrite steel was reproduced. Using the determined material response of the ferrite phase, finite element analyses of the ferrite–pearlite duplex microstructure were executed to scrutinize both the macroscopic material response and microscopic deformation mechanisms. Subsequently, finite element analyses of tensile tests, based on numerical results from microstructural analyses, were carried out to replicate the yield-point phenomena in ferrite–pearlite duplex steels. Consequently, the study characterized the strengthening effect of the pearlite constituent while considering microscopic heterogeneity and yield-point phenomena in the ferrite phase. The findings from the multiscale simulations underscored the necessity for a more accurate estimation of local mechanical properties in both the ferrite phase and pearlite constituent for quantitative simulations.

KEY WORDS: yield-point phenomenon; heterogeneous microstructure; multiscale modeling; ferrite–pearlite duplex steels; finite element method.

1. Introduction

The yield-point phenomenon characterizes a material behavior marked by a distinct yield strength and subsequent stress-drop following the initiation of plastic deformation. It is observed across various materials.[1)] The aforementioned phenomenon is particularly prominent in carbon steels, and the mechanism is believed to be the inhibition of dislocation motion by interstitial atoms such as carbon.[2–4)] During tensile tests, the entire gauge length of the specimen is assumed to be in a uniform uniaxial stress state. However, when a stress-drop is accompanied by the yield-point phenomenon, local deformation occurs and propagates within the gauge length, forming a unique yield plateau in the stress–strain curve.[5)] The stress–strain relationship evaluated by tensile tests included the effects of the specimen shape and size because the yield plateau was caused by non-uniform deformation in the specimen. Thus, the evaluated stress–strain relationship was not a true material response. To address this, numerical methods, such as the finite element method, offer a means to reproduce the stress–strain relationship, considering local deformation due to stress-drop and yield plateau, thereby allowing examination of the true material properties.[6–9)]

Setoyama *et al.*[10,11)] focused on the connectivity of high-strength pearlite microstructures in ferrite–pearlite duplex steels and compared experimental and numerical simulation results. While the yield-point phenomenon manifested in the tensile tests of ferrite–pearlite duplex steel, the stress–strain response of the ferrite single-phase steel, excluding the stress-drop, was employed to establish the stress–strain relationship of the ferrite phase. Watanabe *et al.*[12)] evaluated the mechanical behavior of a multiscale ferrite–pearlite duplex structure using first-principles calculations for cementite. They also utilized a crystal plastic constitutive model based on dislocation density[13)] to characterize the stress–strain relationship for the ferrite phase, encompassing the yield

* Corresponding author: E-mail: WATANABE.Ikumu@nims.go.jp

plateau but omitting the stress-drop. The occurrence of a stress-drop in the ferrite phase of a duplex microstructure, potentially leading to the initiation and propagation of local deformation, has been infrequently discussed in prior studies on numerical simulations.

Watanabe and Iwata[14] proposed an elastoplastic constitutive model that incorporates the yield-point phenomenon to describe the stress-drop. This model features a mathematical structure in which a function describing the general stress–plastic strain relationship is multiplied by an asymptotic function expressing the stress-drop after the onset of yielding. Notably, this allows for a discussion of the steepness of the stress-drop, which has been a facet often overlooked in existing studies. While applying such a constitutive model with a stress-drop to finite element analysis reproduces unstable phenomena with local deformation, numerical simulations can be conducted using the static implicit method, provided that a proper treatment is performed to obtain a stable convergent solution.

Based on the above, in this study, a numerical simulation of tensile tests considering the yield-point phenomena in the elastoplastic constitutive model proposed by one of the authors was performed with simplifications to improve the computational stability and extract the inherent stress–strain relationship of ferrite steel by comparing it with experimental results. Using the stress–strain relationship of the ferrite phase, a deformation simulation of a ferrite–pearlite duplex microstructure was performed to evaluate the deformation state of the microstructure of metallic materials, and the corresponding macroscopic stress–strain relationship and deformation mechanism were discussed. Furthermore, a multiscale analysis was performed to simulate the tensile tests using the macroscopic responses obtained from the numerical simulation of the microstructures of the metallic materials.

2. Constitutive Model

To replicate the yield-point phenomenon through finite element analysis, it is essential to employ an elastoplastic constitutive model that incorporates a stress-drop post the initiation of plastic deformation in the ferrite phase. In this study, a simplified version of the constitutive model proposed by Watanabe and Iwata[14] was utilized. The stress integration algorithm and derivation of the elastoplastic tangential coefficients were formulated in accordance with Watanabe *et al.*[15] The yield-point phenomenon caused a sudden change in the plastic strain along with local deformation. The effect of the strain-rate dependence should be considered; however, for the sake of simplicity, a strain-rate-independent plasticity model was employed.

Based on the finite-strain-elastoplastic theory, elastic-plastic multiplicative decomposition was employed, which is expressed as follows:

$$\boldsymbol{F} = \boldsymbol{F}^{\mathrm{e}}\boldsymbol{F}^{\mathrm{p}} \quad \cdots\cdots (1)$$

where $\boldsymbol{F}$ is the total deformation gradient tensor and $\boldsymbol{F}^{\mathrm{e}}$ and $\boldsymbol{F}^{\mathrm{p}}$ are the elastic and plastic parts of the total deformation gradient, respectively. Using Eq. (1), three bases were defined: reference, intermediate, and current configurations. The St. Venant elastic constitutive model was utilized, which is expressed as follows:

$$\hat{\boldsymbol{S}} = \mathbb{C}^{\mathrm{e}}\frac{1}{2}\left(\boldsymbol{C}^{\mathrm{e}} - \boldsymbol{1}\right) \quad \cdots\cdots (2)$$

where $\hat{\boldsymbol{S}}$ is the second Piola–Kirchhoff stress in the intermediate configuration, $\mathbb{C}^{\mathrm{e}}$ is the elastic tangent coefficient in the intermediate configuration, and $\boldsymbol{C}^{\mathrm{e}}=\boldsymbol{F}^{\mathrm{eT}}\boldsymbol{F}^{\mathrm{e}}$ is the elastic right Cauchy–Green deformation tensor.

In the rate-independent plastic constitutive model, the yield function is defined as

$$\phi = \Sigma - \Gamma \le 0 \quad \cdots\cdots (3)$$

where Σ and Γ are the stress norm and yield stress, respectively. The stress norm Σ corresponding to von Mises stress is defined as follows:

$$\Sigma = \sqrt{\frac{3}{2}\mathrm{dev}\left[\hat{\boldsymbol{T}}\right] : \mathrm{dev}\left[\hat{\boldsymbol{T}}\right]^{\mathrm{T}}} \quad \cdots\cdots (4)$$

where $\hat{\boldsymbol{T}} = \boldsymbol{C}^{\mathrm{e}}\hat{\boldsymbol{S}}$ denotes the Mandel stress in the intermediate configuration. Based on the phenomenological constitutive model proposed by Watanabe and Iwata,[14] yield stress Γ is defined as follows:

$$\Gamma = q\left(1 + r\right) \quad \cdots\cdots (5)$$

where q is a function of internal variables ξ of the plastic deformation history and defines the approximate form of the stress–strain relationship for the plastic loading state including plastic hardening; and r is a function of the internal variable ζ introduced to represent the yield-point phenomenon. In this study, q is defined by the following equation using the Voce-type nonlinear hardening law:[16]

$$q = \tau_{\mathrm{Y}} + \left(\tau_{\mathrm{sat}} - \tau_{\mathrm{Y}}\right)\left(1 - \exp\left[-h\xi\right]\right) + H\xi \quad \cdots\cdots (6)$$

where τ_{Y} is the initial yield stress of the master curve, τ_{sat} is the convergence yield stress when the plastic history variable becomes sufficiently large, h is the sensitivity to nonlinear work hardening, and H is the linear hardening coefficient.

Here, r is defined as a function in which the initial value of Γ is the upper yield stress τ_{Y} and asymptotically approaches zero.

$$r := \left(\frac{\tau_{\mathrm{up}}}{\tau_{\mathrm{Y}}} - 1\right)\exp\left[-k_0\zeta\right] \quad \cdots\cdots (7)$$

where k_0 is the sensitivity of the asymptotic function and ζ is an internal variable describing the variations in the function. Watanabe and Iwata[14] derived an evolution equation for the two internal variables using a formulation based on thermodynamics as follows:

$$\dot{\xi} = -\gamma\frac{\partial\varphi}{\partial q} = \gamma\left(1 + r\right) \quad \cdots\cdots (8)$$

$$\dot{\zeta} = -\gamma\frac{\partial\varphi}{\partial r} = \gamma q \quad \cdots\cdots (9)$$

According to Eq. (7), it is obvious that r has a positive value immediately after yielding. However, it rapidly approaches zero when plastic deformation occurs. Moreover, upon normalizing both sides of Eq. (9) by the initial yield stress τ_{Y}, these are written as:

$$\dot{\xi} \approx \gamma,\ \frac{\dot{\zeta}}{\tau_Y} = \gamma \quad \cdots\cdots (10)$$

Considering the initial values of both variables to be zero, ζ is approximately written as $\zeta = \tau_Y \xi$ and r can be considered as a function of ξ. The sensitivity of the asymptotic function is redefined as $k = \tau_Y k_0$, and the yield stress Γ can be simplified as follows:

$$\Gamma = \left\{\tau_Y + \left(\tau_{sat} - \tau_Y\right)\left(1 - \exp\left[-h\xi\right]\right) + H\xi\right\}\left\{1 + \left(\frac{\tau_{up}}{\tau_Y} - 1\right)\exp\left[-k\xi\right]\right\} \quad \text{..... (11)}$$

The above simplification allows for a single internal variable in the constitutive model and facilitates implementation in the finite element analysis. Thus, it enables robust numerical analysis.

3. Simulation of the Yield-point Phenomenon in Ferrite Steel

Within the yield-point phenomenon, the stress-drop induces the propagation of local deformation, and the stress–strain relationship is influenced by the shape and size of the tensile test. In this study, we conducted numerical simulations of tensile tests, taking into account the yield-point phenomenon observed in experiments. The objective was to determine the plastic properties of the ferrite phase, characterized by a stress-drop.

3.1. Finite Element Model of Tensile Test

A finite-element model of the tensile specimen was prepared based on the tensile test conducted by Setoyama *et al.*[10] (**Fig. 1**). Numerical simulations were performed to apply displacements to the end face of the tensile specimen using the static implicit method, as shown in Fig. 1. In this study, elastic isotropy is assumed and elastic constants are set to be Young's modulus $E = 200$ GPa and Poisson's ratio $\nu = 0.296$ based on the study of Watanabe *et al.*[12] The material constants describing the master curves τ_Y, τ_{sat}, h, and H are set from the latter part of the stress–strain relationship obtained from the tensile test as follows:

$$\tau_Y = 0.095 \text{ GPa},\ \tau_{sat} = 0.305 \text{ GPa},\ h = 40,\ H = 0.33 \text{ GPa}$$

The upper yield stress was set to be $\tau_Y = 0.354$ GPa based on the experimental data of Setoyama *et al.*[10] The parameter k was determined to minimize the differences in the stress–strain curves obtained from the experiments and simulations.

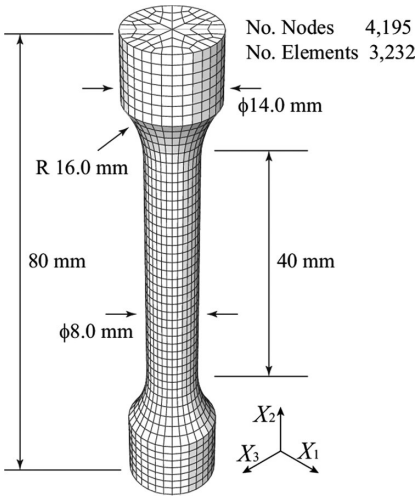

Fig. 1. Finite element model of the tensile specimen.

3.2. Simulation Results and Parametric Study

Owing to the propagation of local deformation throughout the entire specimen during the yield-point phenomenon, the strain range of the yield plateau in the stress–strain relationship is not solely dependent on material constants but also influenced by the size of the specimen. Consequently, evaluating the true mechanical properties of ferrite steels involves performing numerical simulations of tensile tests using a finite element model that aligns with experimental results and determines the material constants. In line with the experiment, the stress–strain relationship in the numerical simulation was converted to the true stress–strain relationship by deriving the nominal stress-nominal strain relationship from the load–displacement relationship and specimen dimensions. The responses of the constitutive model (11) to changes in the material constant k are illustrated in **Fig. 2**(a). The stress–strain relationship calculated from the numerical simulation of the tensile test, alongside the corresponding experimental results, is shown in Fig. 2(b). In addition, the stress–strain relationship evaluated from the results of numerical simulations of the tensile tests using this constitutive model showed a distinct yield plateau. In other words, the stress–strain relationship shown in **Fig. 3**(b), calculated from the numerical simulation of the tensile test, gives a completely different response from that of the constitutive equation (Eq. (11)). To determine the appropriate material constant k corresponding to the experimental results, a residual error between the experimental and constitutive model responses was defined and minimized using the equation:

$$\Delta = \frac{1}{\tau_Y}\int_{\varepsilon}\left|\Sigma^{\varepsilon}_{exp} - \Sigma^{\varepsilon}_{sim}\right| d\varepsilon \quad \text{..... (12)}$$

where $\Sigma^{\varepsilon}_{exp}$ and $\Sigma^{\varepsilon}_{sim}$ are the stress norm values of experiments and numerical simulations at axial strain ε, in which von Mises stress norm corresponds to the axial stress value in a tensile test. In this study, the residual norm was evaluated by numerical integration in the axial strain range $\varepsilon \in [0.01,\ 0.05]$ where a yield plateau appeared. The relationship between the evaluated material constant k and the residual norm is illustrated in Fig. 3, aiding in determining the appropriate parameters.

It is evident that the numerical simulation, utilizing the determined material constants, reproduces the experimental stress–strain relationship as shown in Fig. 2(b). The distributions of equivalent plastic strain and equivalent stress in the strain region of $\varepsilon \in [0.01,\ 0.05]$ are shown in **Fig. 4**. It can be seen that the stress-drop after the upper yield point causes local deformation which propagates through the region. In this study, any imperfections were given to the finite element model for controlling the initiation area of yielding; therefore, yielding occurs at a point in the tensile specimen where the stress is slightly higher at a numerical precision level. In the region of yield plateau, the specimen is non-uniformly deformed, but when the entire gauge length undergoes plastic deformation with stress-drop, the entire specimen becomes uniformly deformed.

For problems involving local deformation, such as yield-point phenomena, the dependence on finite element mesh

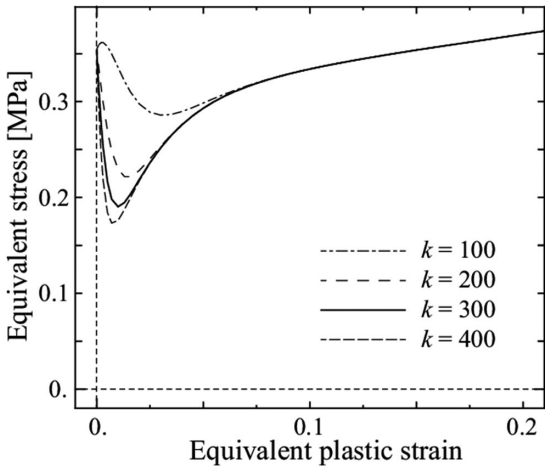

(a) Constitutive model

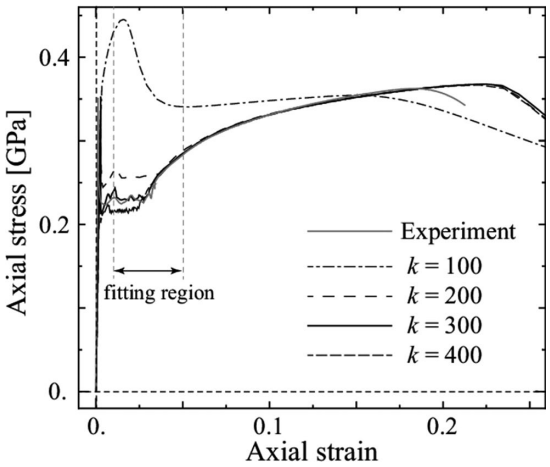

(b) Finite element analysis

Fig. 2. Sensitivity of parameter k on stress–strain curves.

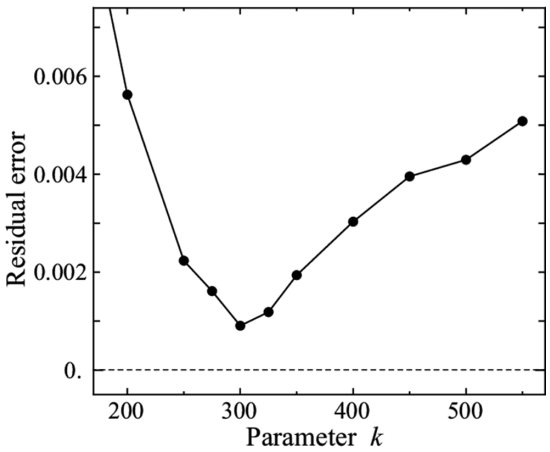

Fig. 3. Residual error in finite element analyses changing parameter k.

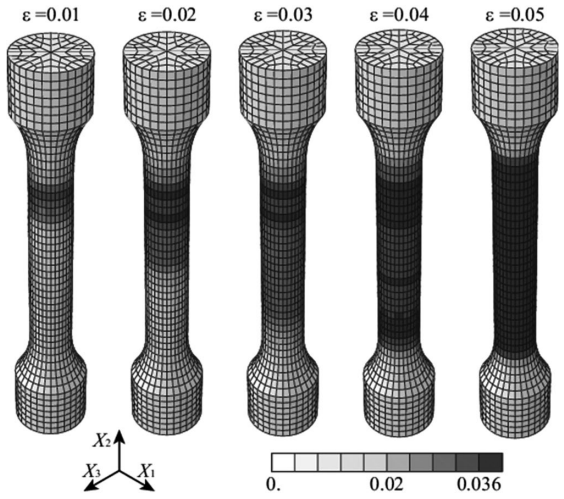

(a) Equivalent plastic strain

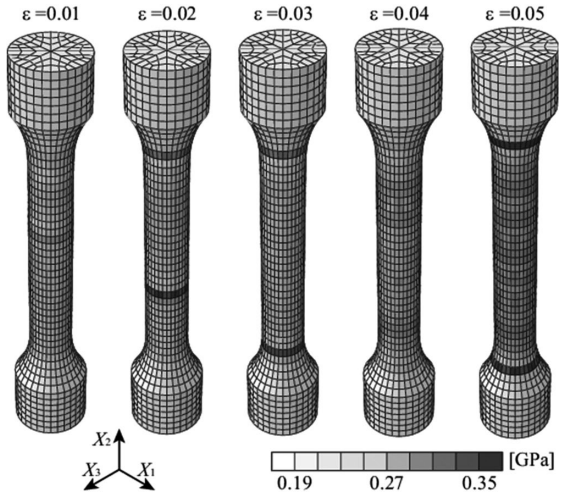

(b) Equivalent stress

Fig. 4. Numerical results: finite element analyses of the tensile test.

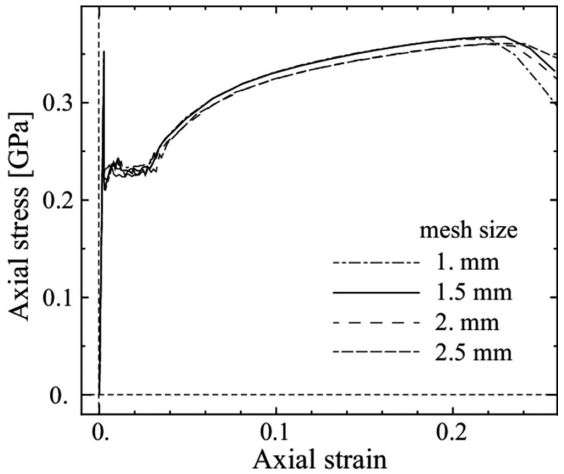

Fig. 5. Mesh sensitivity of finite element analyses in tensile test.

resolutions becomes significant. **Figure 5** demonstrates the change in the stress–strain relationship when varying the size of finite element discretization for the determined material constants. When the mesh is coarse, the material response after the yield plateau is different. The finite element model with a mesh size of 1.5 mm was adopted in this study, as models with a mesh size of 1.0 mm and 1.5 mm exhibited nearly identical responses.

In conclusion, by determining the material constants in the constitutive model (11) to minimize the difference between experimental and numerical simulations, the material response, including the stress-drop leading to the yield plateau, can be accurately extracted.

4. Multiscale Simulation of Ferrite–Pearlite Duplex Structure

Using the stress–strain relationship of the ferrite phase,

including the stress-drop determined in the previous section, finite element analyses of the ferrite–pearlite duplex structure were performed to determine the effect of the stress-drop of the ferrite phase on the macroscopic stress–strain relationship. Numerical simulations of the tensile tests were performed using the obtained macroscopic stress–strain relationships, and the results were compared with the experimental results. Samples with pearlite volume fractions of 21.5% and 40.3% in the experimental results of Setoyama *et al.*[10] were considered for the analysis.

4.1. Finite Element Models of Duplex Microstructure

Finite element models of the ferrite–pearlite duplex microstructure, aligning with the experimental setup, were created, as depicted in **Fig. 6**. The overall region in Fig. 6 comprises 54 truncated octahedra under a periodic boundary condition. Each truncated octahedron is subdivided into 48 units of the same shape for symmetry, resulting in a total of 2 592 units. Additionally, each unit is further divided into six eight-node hexahedral elements. This finite element model enables a more random distribution of the ferrite phase and pearlite constituent, offering more precise control over the volume fraction compared to the model by Setoyama *et al.*[10] Deformation analyses were conducted by imposing a macroscopic displacement gradient based on finite element analysis for a representative volume element.[12]

The stress–strain relationship derived in the preceding section was utilized to determine the mechanical properties of the ferrite phase. Regarding the elastic properties of the pearlite constituent, specifically Young's modulus E_P and Poisson's ratio ν_P, the values obtained from the multiscale analysis in Watanabe *et al.*[12] were employed.

$$E_P = 216 \text{ GPa}, \nu_P = 0.288 \quad \text{..... (13)}$$

The plastic properties of the pearlitic microstructure were based on the stress–plastic strain relationship derived from the experimental data used by Setoyama *et al.*[10]

4.2. Results and Discussion

Initially, the finite element model illustrated in Fig. 6 underwent the imposition of macroscopic strain modes corresponding to the six strain components. This step aimed to validate its status as a representative volume element, and the resulting elastic tangent coefficients were assessed. The numerical outcomes are detailed in **Table 1**. The attainment of isotropic elastic tangent coefficients for both finite element models suggests that the model in Fig. 6 exhibits adequate random heterogeneity, affirming its suitability as a representative volume element. To ensure robustness, the macroscopic displacement gradient was manipulated to achieve a macroscopic uniaxial stress state in the Y_1, Y_2 and Y_3 axial directions, and this condition was sustained up to a high strain. The macroscopic equivalent stress–strain relationship obtained from the numerical analysis is shown in **Fig. 7**(a). The equivalent strain is defined as

$$\varepsilon^* = \sqrt{\frac{2}{3}\mathrm{dev}[\boldsymbol{\varepsilon}] : \mathrm{dev}[\boldsymbol{\varepsilon}]} \quad \text{..... (14)}$$

where $\boldsymbol{\varepsilon}$ is defined as $\boldsymbol{\varepsilon} = \frac{1}{2}\ln\left[\boldsymbol{F}\boldsymbol{F}^{\mathrm{T}}\right]$. As in the elastic response, the macroscopic stress–strain relationships in each triaxial direction were almost identical; thus, only the results in the Y_1 axis direction are shown, as in the evaluation of Setoyama *et al.*[10] In the macroscopic stress–strain relationship of both finite element models with different volume fractions of pearlite constituent, a stress-drop is observed after yielding; however, as shown in **Table 2**, the increment in the upper yield stress due to compositing is relatively small considering the strength difference between the ferrite phase and pearlite constituent. This is because after the yield of the ferrite phase, plastic deformation rapidly progresses with local deformation, and the yield strength of the entire duplex structure is determined by the upper yield stress of the ferrite phase. In other words, assuming that the elastic strains ε^e of the ferrite phase and pearlite constituent coincide because the deformation is almost uniform in the elastic range, the yield stress of the ferrite–pearlite duplex microstructure when the ferrite phase reaches the stress value at the upper yield-point can be expressed by the following equation using the mean field theory:

$$\begin{aligned}\bar{\sigma}_Y &= (1-f)\sigma_{up} + f\sigma_P = \left\{(1-f)E_F^* + fE_P^*\right\}\varepsilon_{up}^e \quad \text{... (15)}\\ &= \left\{(1-f) + f\frac{E_P^*}{E_F^*}\right\}\sigma_{up}\end{aligned}$$

where f is the volume fraction of pearlite constituent, σ_P is the equivalent stress value when the ferrite phase reaches the upper yield stress, and E_F^* and E_P^* are the equivalent elastic stiffness of the ferrite phase and pearlite constituent calculated as follows:

$$E_F^* = \frac{3E_F}{2(1+\nu_F)} = 231.48 \text{ GPa}, E_P^* = 251.55 \text{ GPa} \quad \text{... (16)}$$

Therefore, the yield stress of the ferrite–pearlite duplex microstructure was estimated using the following equation:

$$\bar{\sigma}_Y = (1 + 0.0867f)\sigma_{up} \quad \text{..... (17)}$$

The estimated values of the upper yield stress correspond-

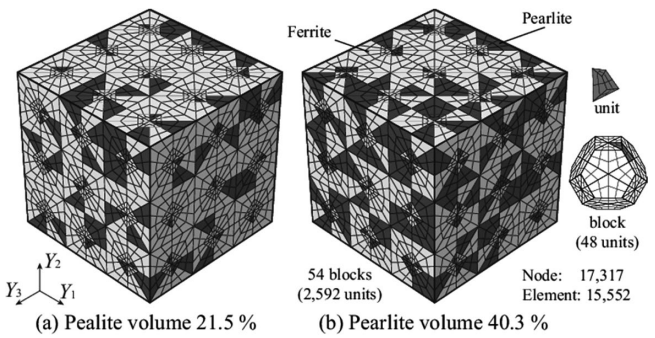

Fig. 6. Finite element models of the ferrite–pearlite duplex microstructure.

Table 1. Elastic constants estimated with finite element analyses of the ferrite–pearlite duplex microstructure.

Pearlite volume fraction	$\bar{\mathbb{C}}^e_{iiii}$	$\bar{\mathbb{C}}^e_{iijj} = \lambda$	$\bar{\mathbb{C}}^e_{ijij} = \mu$	E	ν
21.5%	269.49	112.38	78.56	203.4	0.2943
40.3%	272.34	112.75	79.80	206.3	0.2928

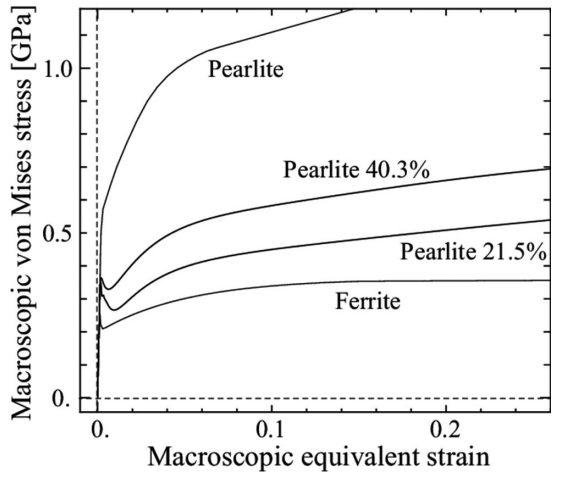

(a) Microstructure

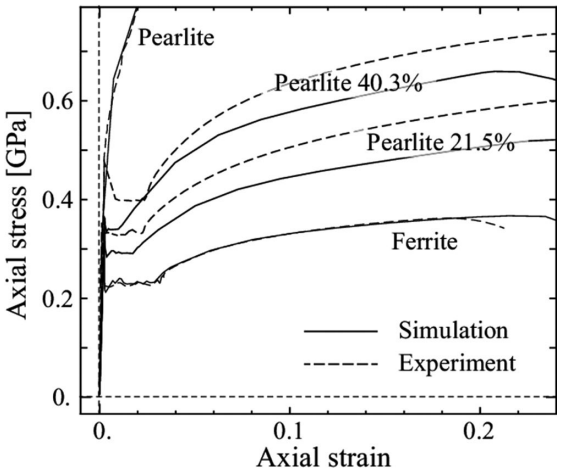

(b) Tensile test

Fig. 7. Numerical results: stress–strain curves of the ferrite–pearlite duplex steels.

ing to the finite element model are presented in Fig. 6 and summarized in Table 2. The stress-drop after yielding in the stress–strain relationship became more gradual as the volume fraction of pearlite constituent increased, and the stress-drop could not be confirmed in the region where the volume fraction of pearlite constituent exceeded 50%.

To examine the deformation state of the ferrite–pearlite duplex microstructure during the stress-drop, the distribution of equivalent plastic strain in the macroscopic equivalent strain range $\varepsilon^* \in [0.003, 0.01]$ is illustrated in **Fig. 8**. In the finite-element model with a pearlite volume fraction of 21.5%, local deformation propagated in the ferrite phase and extended across the microstructure, transitioning to deformation of the entire region. In contrast, in the finite element model with a pearlite volume fraction of 40.3%, local deformation occurred, but the propagation of this local deformation was hindered by the pearlite constituent. Consequently, the impact of the stress-drop on the macroscopic stress–strain relationship diminished with an increasing pearlite volume fraction. Leveraging the macroscopic stress–strain relationship of the ferrite–pearlite duplex microstructure obtained through numerical analysis, finite element analyses of the tensile test were executed using the finite element model depicted in Fig. 1. The results of the numerical simulation of the tensile test and the correspond-

Table 2. Yield strength calculated with finite element analyses of the ferrite–pearlite duplex microstructure.

Pearlite volume fraction	Numerical result	Estimation
0%	0.354 GPa	0.354 GPa
21.5%	0.357 GPa	0.361 GPa
40.3%	0.364 GPa	0.366 GPa

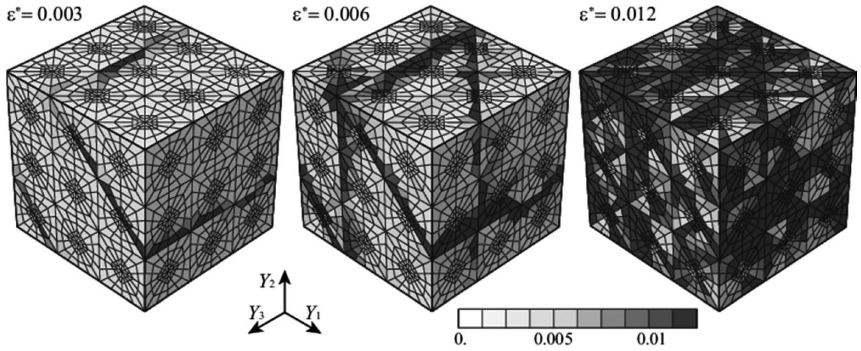

(a) Pearlite volume 21.5%

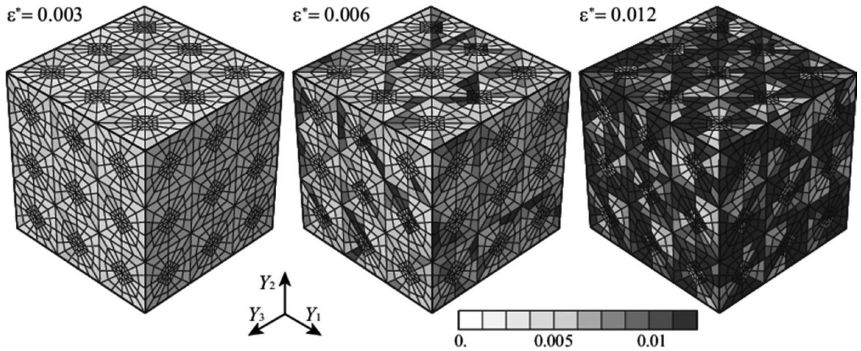

(b) Pearlite volume 40.3%

Fig. 8. Numerical results: distribution of the equivalent plastic strain in the ferrite–pearlite duplex steels.

ing experimental results are displayed in Fig. 7(b). The yield-point phenomenon was successfully reproduced based on the macroscopic stress–strain relationship derived from the ferrite–pearlite duplex microstructure. This multiscale numerical simulation elucidated the mechanism whereby the yield-point phenomenon was less likely to occur in tensile tests owing to the constraint of local deformation in the ferrite phase within the microstructure as the volume fraction of the pearlite constituent increased.

Using the macroscopic stress–strain relationship of the ferrite–pearlite duplex microstructure obtained by numerical analysis, finite element analyses of the tensile test were performed using the finite element model shown in Fig. 1. The results of the numerical simulation of the tensile test and the corresponding experimental results are shown in Fig. 7(b). The yield-point phenomenon was reproduced based on the macroscopic stress–strain relationship evaluated from the ferrite–pearlite duplex microstructure. In this study, a multiscale numerical simulation reproduced the mechanism by which the yield-point phenomenon was less likely to appear in tensile tests by constraining the local deformation in the ferrite phase in the microstructure as the volume fraction of the pearlite constituent increased.

The experimental stress–strain relationship showed higher stress values than the numerical simulation and did not reproduce the phenomenon quantitatively. This discrepancy can be attributed to the inherent differences in properties between each phase and the microstructure of the target ferrite–pearlite duplex microstructure compared to the ferritic single-phase and pearlite steels used to define the material properties in the numerical simulation. Equation (17) highlights the necessity for an increase in the upper yield stress of the ferrite phase to align with the experimental yield stress. For duplex steel with a volume fraction of pearlite constituent of 40.3%, the estimated increase in the yield stress is approximately 0.5 GPa to match the reference yield stress. This suggests that the mechanical properties of the ferrite phase in duplex steel significantly differ from those of the ferrite single-phase steel used in this study. Consequently, to model the ferrite–pearlite duplex structure accurately, it is imperative to assess local mechanical properties through microscopic material tests.[17–19] For example, a method for evaluating local mechanical properties by coupling microindentation tests with numerical simulations have been proposed.[20,21] It is expected that extending the method to stress–strain relationships with stress-drop will be useful for addressing this problem.

5. Conclusion

In this study, we investigated the yield-point phenomenon observed in the tensile tests of ferrite–pearlite duplex steel through multiscale numerical simulations, accounting for nonuniform deformation of the specimen and material microstructure. The true stress–strain relationship of the ferrite phase was discerned by replicating the yield-point phenomenon using numerical simulations. We examined the deformation mechanism of the ferrite–pearlite duplex microstructure, which exhibited the yield-point phenomenon, based on the mechanical properties of the ferrite phase. Furthermore, a numerical simulation of the microstructure of the material successfully reproduced the yield-point phenomenon observed in the tensile tests of ferrite–pearlite duplex steel. The numerical analyses conducted on the duplex microstructure provided the macroscopic stress–strain relationship, effectively capturing the yield-point phenomenon in the tensile tests. Despite the inherent challenges associated with numerically simulating unstable phenomena characterized by local deformation, such as the yield-point phenomenon, recent advancements in numerical analysis techniques have made it feasible. An evaluation method that integrates experimental data with numerical simulations proves valuable for comprehending the mechanisms underlying material instability phenomena.

Acknowledgments

This study was supported financially by KAKENHI 21H01220. The authors thank Dr. Daigo Setoyama at Toyota Central R&D Labs, Inc. for providing the experimental data.

We also thank Ms. Yuki Yamamoto and Dr. Sachiko Taniguchi of the National Institute for Materials Science for their invaluable technical assistance in developing the numerical model.

REFERENCES

1) E. O. Hall: Yield Point Phenomena in Metals and Alloys, Springer, New York, NY, (1970). https://doi.org/10.1007/978-1-4684-1860-6
2) A. H. Cottrell and B. A. Bilby: *Proc. Phys. Soc., A*, **62** (1949), 49. https://doi.org/10.1088/0370-1298/62/1/308
3) W. M. Lomer: *J. Mech. Phys. Solids*, **1** (1952), 64. https://doi.org/10.1016/0022-5096(52)90007-0
4) W. G. Johnston and J. J. Gilman: *J. Appl. Phys.*, **30** (1959), 129. https://doi.org/10.1063/1.1735121
5) G. T. Hahn: *Acta Metall.*, **10** (1962), 727. https://doi.org/10.1016/0001-6160(62)90041-X
6) J. A. Shaw and S. Kyriakides: *Int. J. Plast.*, **13** (1997), 837. https://doi.org/10.1016/S0749-6419(97)00062-4
7) H. Tsukahara and T. Iung: *Mater. Sci. Eng. A*, **248** (1998), 304. https://doi.org/10.1016/S0921-5093(97)00857-5
8) F. Yoshida, Y. Kaneda and S. Yamamoto: *Int. J. Plast.*, **24** (2008), 1792. https://doi.org/10.1016/j.ijplas.2008.05.004
9) R. Schwab and V. Ruff: *Acta Mater.*, **61** (2013), 1798. https://doi.org/10.1016/j.actamat.2012.12.003
10) D. Setoyama, I. Watanabe and N. Iwata: *Tetsu-to-Hagané*, **98** (2012), 290 (in Japanese). https://doi.org/10.2355/tetsutohagane.98.290
11) I. Watanabe, G. Nakamura, K. Yuge, D. Setoyama and N. Iwata: From Creep Damage Mechanics to Homogenization Methods, Advanced Structured Materials Vol. 64, Springer, Cham, (2015), Chapter 24, 541. https://doi.org/10.1007/978-3-319-19440-0_24
12) I. Watanabe, D. Setoyama, N. Nagasako, N. Iwata and K. Nakanishi: *Int. J. Numer. Methods Eng.*, **89** (2012), 829. https://doi.org/10.1002/nme.3264
13) I. Watanabe, D. Setoyama, N. Iwata and K. Nakanishi: *Int. J. Plast.*, **26** (2010), 570. https://doi.org/10.1016/j.ijplas.2009.09.005
14) I. Watanabe and N. Iwata: *Tetsu-to-Hagané*, **100** (2014), 1232 (in Japanese). https://doi.org/10.2355/tetsutohagane.100.1232
15) I. Watanabe, N. Iwata and K. Nakanishi: *Trans. Jpn. Soc. Comput. Eng. Sci.*, **2010** (2010), 20100005 (in Japanese). https://doi.org/10.11421/jsces.2010.20100005
16) E. Voce: *J. Inst. Met.*, **74** (1948), 537.
17) R. Ando, T. Matsuno, T. Matsuda, N. Yamashita, H. Yokota, K. Goto and I. Watanabe: *ISIJ Int.*, **61** (2021), 473. https://doi.org/10.2355/isijinternational.ISIJINT-2020-546
18) Y. Tampa, K. Takagi, S. Ueki, M. Ohta, Y. Mine and K. Takashima: *ISIJ Int.*, **62** (2022), 1741. https://doi.org/10.2355/isijinternational.ISIJINT-2022-088
19) V. Jayaram: *Annu. Rev. Mater. Res.*, **52** (2022), 473. https://doi.org/10.1146/annurev-matsci-080819-123640
20) K. Goto, I. Watanabe and T. Ohmura: *Int. J. Plast.*, **116** (2019), 81. https://doi.org/10.1016/j.ijplas.2018.12.007
21) T.-T. Chen and I. Watanabe: *Sci. Technol. Adv. Mater.-Methods*, **2** (2022), 416. https://doi.org/10.1080/27660400.2022.2129508